

Halide segregation versus interfacial recombination in bromide-rich wide-gap perovskite solar cells

Francisco Peña-Camargo¹, Pietro Caprioglio^{1,2}, Fengshuo Zu^{3,4}, Emilio Gutierrez-Partida¹, Christian M. Wolff¹, Kai Brinkmann⁵, Steve Albrecht², Thomas Riedl⁵, Norbert Koch^{3,4}, Dieter Neher¹, Martin Stolterfoht^{1,*}

¹Institute of Physics and Astronomy, University of Potsdam, Karl-Liebknecht-Str. 24-25, D-14476 Potsdam-Golm, Germany.

²Young Investigator Group Perovskite Tandem Solar Cells, Helmholtz-Zentrum Berlin für Materialien und Energie GmbH, Kekuléstraße 5, 12489 Berlin, Germany

³Helmholtz-Zentrum Berlin für Materialien und Energie GmbH, 12489 Berlin, Germany

⁴Institut für Physik & IRIS Adlershof, Humboldt-Universität zu Berlin, 12489 Berlin, Germany

⁵Institute of Electronic Devices, University of Wuppertal, Rainer-Gruenter-Str 21, 42119 Wuppertal, Germany

email: stolterf@uni-potsdam.de

Abstract

Perovskites offer exciting opportunities to realise highly efficient multi-junction photovoltaic (PV) devices in combination with various established and emerging PV technologies, set to overcome the fundamental limitations of single-junction solar cells. To this end, high- V_{OC} and often Br-rich perovskite cells are required, which currently suffer from severe limitations commonly attributed to halide segregation. Here, we study efficient triple cation perovskite cells over a wide bandgap range (~ 1.5 eV - 1.9 eV). While, all studied wide-gap cells (≥ 1.69 eV) experience rapid phase segregation under illumination (seconds), the electroluminescence spectra are less affected by this process. The measurements reveal a low electroluminescence quantum yield of the mixed halide perovskite phase which explains the significant V_{OC} losses with increasing Br-content. Photoluminescence measurements on fresh, partial cell stacks prior to significant halide segregation reveal that both transport layer (PTAA and C_{60}) cause a significant reduction in PL yield in Br-rich ($>30\%$) samples. The findings confirm that the presence of the segregated iodide-rich domains is not directly responsible for the low V_{OC} , but the significant non-radiative recombination at the interfaces. Consistent with this, LiF can improve the V_{OC} of cells that are primarily limited by the n -interface (≤ 1.75 eV) resulting in 20% efficient 1.7 eV bandgap cells. However, a simultaneous optimization of the hole transport layer or p -interface is necessary to further advance even larger bandgap (≥ 1.75 eV) pin -type cells in the future.

Introduction

Perovskites have attracted enormous research interests due to their ease of fabrication and favourable opto-electronic properties such as defect tolerant nature,¹ and near ideal optical and emissive properties.² This renders them highly interesting for a range of applications including photodetectors^{3,4}, LEDs^{5,6} and solar cells.⁷⁻⁹ In particular, perovskite-based multi-junction solar cells are among the fastest growing research topics in the perovskite community as the simple processability from solution^{10,11} or vacuum deposition^{12,13} opens a range of new tandem applications. These combinations include perovskite/quantum dot solar cells,^{14,15} perovskite/organic photovoltaics,¹⁷ perovskite/perovskite,^{18,19} silicon/perovskite,²⁰⁻²² CIGS/perovskite^{23,24} and other combinations with established thin film technologies.²⁵⁻²⁷ Of particular interest for all these tandem solar cells are wide bandgap perovskites, here defined with a bandgap ≥ 1.7 eV.²⁸ For example, a

perovskite with a bandgap of around 1.7 eV is the ideal candidate for monolithic Si/perovskite tandem cells while a bandgap of 1.8 eV is suitable for perovskite/perovskite tandem cells due to the current bandgap limitation of mixed Sn/Pb based perovskites at a minimal bandgap of ~ 1.2 eV.¹⁹ Depending on the achievable short-circuit current of the low-gap partner cell, or the number of junctions, even higher bandgap perovskites may be useful for multijunction cells.

A common, well-known approach to tune the bandgap is to substitute the ions on the X-site of the ABX_3 perovskite structure.²⁹ For lead-based perovskites, $APb(I_xBr_y)$, this allows to increase the bandgap from ~ 1.5 eV when A=formamidinium and $x=1$ (pure iodine) to 2.35 eV when A=methyl ammonium and $y=1$ (pure bromine).³⁰ Although the substitution of iodine by bromine does, in fact, shift the absorption onset,³¹ as soon as the bromine proportion exceeds a critical value, increasing the bandgap does not translate into a corresponding increase in the V_{OC} as depicted in **Figure 1a**. In the community, this phenomena is known as the *Hoke limit*,³² who first observed the formation of a photo-induced low energy peak during photoluminescence (PL) measurements and attributed this to the segregation of halides into small physical domains.³³ Because of the correlation between the photo-induced segregation effect and the pinning of the V_{OC} , it was subsequently assumed that the halide segregation is responsible for the open-circuit voltage losses with increasing bandgap. However, very recently this interpretation has become under debate again. In particular, Mahesh et al.³⁰ argued that the halide segregation is not the critical limitation but the low initial electroluminescence quantum yield (EQE_{EL}) of the non-segregated phase. This conclusion was based on an estimation of the initial electroluminescence quantum yield of a wide-gap cell (e.g. $\sim 1 \times 10^{-6}$ for a 1.77 eV gap cell) by comparing the measured V_{OC} with the radiative open-circuit voltage. The loss due to the halide segregation was then quantified from the increased sub-gap absorption from the iodide-rich domains during constant illumination which increases the *radiative* V_{OC} losses. The authors concluded that the low initial EQE_{EL} yield of the non-segregated cell dominates the voltage losses (e.g. 385 mV for the 1.77 eV cell), while the additional radiative V_{OC} loss due to the halide segregation was much smaller (e.g. 75 mV). However, the EQE_{EL} yield was not experimentally measured and it remains unclear whether the halide-induced segregation loss can be fully captured from the increase in the radiative recombination current due to extended device absorption or if there are other non-radiative losses associated to halide-segregation influencing the low, initial EQE_{EL} . For example, Br-rich samples may be partially phase segregated but the impact on the absorption or EQE_{PV} absorption could negligibly small and barely detectable. Moreover, the segregation could lead to enhanced non-radiative recombination before the halide segregation appears in the absorption spectrum.

However, these new interesting developments raise the important question whether it is actually a bulk property (e.g. defects) or indirectly the segregation of halides that limits the open-circuit voltage of these wide bandgap *pin*-type cells, or if there are other dominant recombination processes. For example, the halide segregation could reduce the radiative efficiency of the neat material due to increased non-radiative recombination in the bulk or at the surface and thus change the relative importance of bulk recombination with respect to the recombination at the interfaces. The latter been demonstrated to be the main performance limitation in *pin*-type triple cation perovskite cells with a bandgap close to 1.6 eV.³⁴ Moreover, both or one particular interface could deteriorate with increasing Br-content. Another aspect that should be taken into account is the change of energy level alignment between the perovskite (valence and conduction) bands and the transport layers when the bandgap of the absorber layer changes. In this regard, using ultraviolet photoelectron spectroscopy (UPS), we have recently shown that the valence band maximum of $CS_{0.05}(FA_{0.83}MA_{0.17})_{0.95}Pb(I_{0.83}Br_{0.17})_3$ triple cation cells with a bandgap of 1.63 eV is well aligned with the hole-transporting layer.³⁵ This is consistent with the match between the external V_{OC} and the internal voltage (i.e. the quasi-Fermi level splitting) in the perovskite layer, which suggests that both transport layers (PTAA and C_{60}) are

energetically aligned.³⁶ However, this alignment may be impaired when the bandgap of the absorber layer increases (while keeping the same transport layers).

In order to address the above raised questions, we have studied *pin*-type triple cation perovskite solar cells as a model system over a wide range of bandgaps from 1.53 eV to 1.88 eV. In terms of photovoltaic performance, we observed - not unexpectedly - a saturation of the V_{OC} to approximately 1.17 V when increasing the bandgap beyond 1.53 eV to up to 1.9 eV. In order to elucidate the reasons behind this common observation in literature, we performed absolute photoluminescence (PL) and electroluminescence (EL) measurements. Interestingly, while the PL of complete cells behaved as expected considering the above described findings in literature, with a red-shifted peak emission at around 1.55 eV, the EL spectrum was very different. In fact, the peak of the EQE_{EL} followed within a relatively small uncertainty the bandgap of the mixed halide phase, allowing to directly assess its radiative efficiency (i.e. the nominal composition of the absorber layer). The results showed a strong reduction in EQE_{EL} yield when increasing the bandgap, which confirms that the primary limitation is due to strong non-radiative recombination in the mixed halide phase which caps the V_{OC} of the cells to a certain value. To further investigate the reason behind the low EQE_{EL} yield, we measured the PL-yield on partial solar cell stacks fast enough to prevent the occurrence of significant halide segregation. These measurements demonstrate a significant drop in the PLQY of the mixed phase in the presence of either transport layer, in particular in the case of the hole transport layer when the Br concentration increases beyond $\approx 30\%$. This explains why improvements at the top interface (e.g. using LiF) fail at even higher Br concentrations and bandgaps as in this case, the recombination at the *p*-interface becomes limiting. We conclude that the presence of the iodide-rich domains is not the primary reason for the observed V_{OC} loss, rather a comparatively high interfacial defect density in the mixed halide phase and partially energy alignment issues.

Results

We fabricated several perovskite solar cells in the *pin*-structure of [ITO (150 nm)/PTAA:PFN-Br (8 nm)/perovskite (400 nm)/C₆₀ (30 nm)/BCP (8nm)/Cu (100 nm)], where ITO is indium tin oxide, PTAA is poly[bis(4-phenyl)(2,4,6-trimethylphenyl)amine], PTAA-Br is poly[(9,9-bis(30-((N,N-dimethyl)-N-ethylammonium)-propyl)-2,7-fluorene)-alt-2,7-(9,9-dioctylfluorene)] dibromide, BCP is bathocuproine and *perovskite* stands for a triple cation composition consisting of Cs_{0.05}(FA_xMA_y)_{0.95}Pb(I_xBr_y)₃, where $x = 1-y$ ranges from 0.5 to 1.0. As discussed previously, the absorption onset is directly related to the bromine/iodine ratio at the X site of the perovskite structure ABX₃. **Figure 1b** shows the normalised EQE_{PV} curves which demonstrates the increasing bandgap with the increasing Br ratio. The summary of the parameters for all fabricated devices is shown in **Figure 1c**. It is clear that the losses in power conversion efficiency are mainly due to losses in V_{OC} , which does not follow the increase in bandgap, but plateaus at approximately 1.17 V when the proportion of bromine surpasses 30% (i.e. when $x=0.70$) consistent with recent reports.²⁸

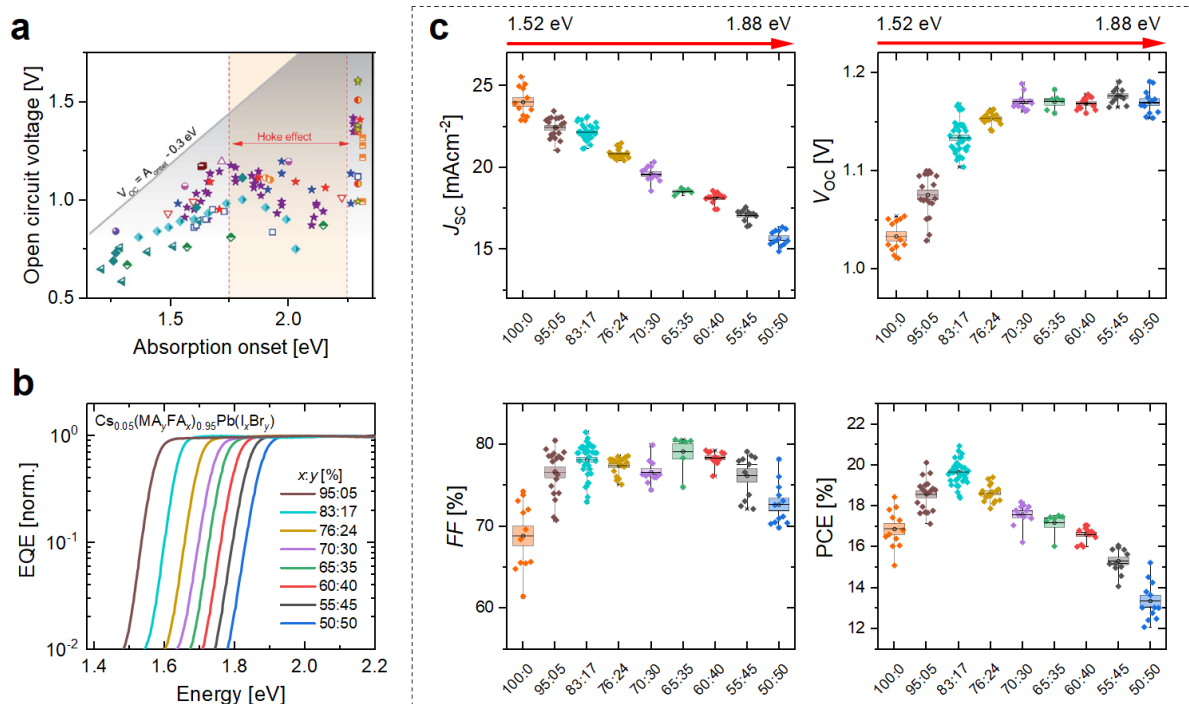


Figure 1. **a**, The open-circuit voltage deficit (highlighted in orange) observed in literature for perovskite compositions with bandgaps from 1.75 eV to 2.25 eV, which has been ascribed to the Hoke effect. Notably, there are already exceptions to this trend, however, to our knowledge only in *nip*-type cells.³⁷ Data adapted from ref.,²⁸ permission pending. **b**, Normalised external quantum efficiency (EQE_{PV}) for all the studied compositions for triple cation perovskite solar cells with stoichiometry of $\text{Cs}_{0.05}(\text{FA}_x\text{MA}_y)_{0.95}\text{Pb}(\text{I}_x\text{Br}_y)_3$, where $x=1-y$ was varied from 0.5 to 1.0. **c**, Corresponding solar cell performance, highlighting that the V_{oc} does not increase at bandgaps larger than 1.63 eV, which confirms the observations in literature for the studied perovskite system. Ultimately, the saturation in V_{oc} leads to a significant drop in the perovskite solar cell performance at bandgaps greater than 1.63 eV.

To investigate the potential impact of halide segregation, we first performed photoluminescence (PL) measurements on the complete cells under a 1 sun equivalent illumination, following our previous approach. As shown in **Figure 2a**, we found that although the bandgap shifts as expected with the Br-content, the steady-state peak emission is independent on the studied composition and it is centred at ~ 1.55 eV. Whilst this is quite unexpected for solar cell technologies, for wide bandgap perovskites it is not. The constant PL peak position indicates that regardless of the perovskite composition, the emission comes from an iodide-rich domain with a lower bandgap below 1.6 eV. Notably, very similar findings have been reported in various recent papers.^{33,38,39} Moreover, the PL intensity reduces with increasing bandgap, something that will be discussed further below. We note that the PL was measured on cells that were characterised with *JV* measurements one day earlier and the samples were illuminated for around 10 seconds before recording the PL spectra. This suggests that the samples immediately phase-segregate during initial *JV* measurement which will be discussed further below. On the other hand, the absence of an absorption feature in the EQE_{PV} spectra (until 10^{-2}) in **Figure 2a** indicates that the volume fraction covered by the segregated domains is relatively small as they would otherwise be noticeable in the EQE_{PV} spectra as shown, for instance, in reference.³⁰ In order to investigate this further, we recorded the EQE_{PV} spectra close to 10^{-4} as shown in the **Supplementary Figure S1** and found no additional prominent feature in the subgap regime. To test whether this halide segregation becomes visible in the EQE spectra, we illuminated the cells for 30 minutes under the simulated AM1.5G sun spectrum (that of our *JV* measurement setup) and recorded the EQE_{PV} once more (**Supplementary Figure S1**). Again, no additional feature in the EQE was observed after the illumination, further consistent with the assumption that the iodide rich domains did not significantly contribute to the absorption or charge collection. This highlights the absence of additional

recombination losses in this type of cells due to the halide segregation.³⁰ At this point, we also note that the PCE of the cells did not change significantly after several months of dark storage (**Supplementary Figure S2**). Moreover, **Supplementary Figure S3** presents the maximum power point tracking for 60 minutes. This shows that the samples are relatively stable on these timescales despite the presence of the halide segregation in the PL.

In the next step, we performed electroluminescence measurements as shown in **Figure 2b** under carrier concentrations comparable to 1 sun illumination, i.e. where the injection current is approximately equal to the short-circuit current. The spectra in **Figure 2b** are normalized whilst **Supplementary Figure S4a** shows the original ones. Very surprisingly (and in contrast to the PL measurements), we find that the electroluminescence spectra follow the same trend as the EQE_{PV} which means that it is the emission from the mixed perovskite phase which governs the absorption.⁴⁰ It is worth clarifying that both the electroluminescence flux and the external electroluminescence quantum efficiency were taken on the same samples one day after measuring the photoluminescence spectra. Therefore, we can exclude that the difference between the EQE_{EL} and the PL spectra is due to a sample to sample variation. Overall, the results indicate that in the EQE_{EL} measurements, the occupation of the low bandgap states corresponding to the iodide-rich domains is very low and hence, does not result in an appreciable contribution to the EL spectrum. Although this is certainly surprising, we have not yet found the exact reason for this interesting observation and this is subject of ongoing work.

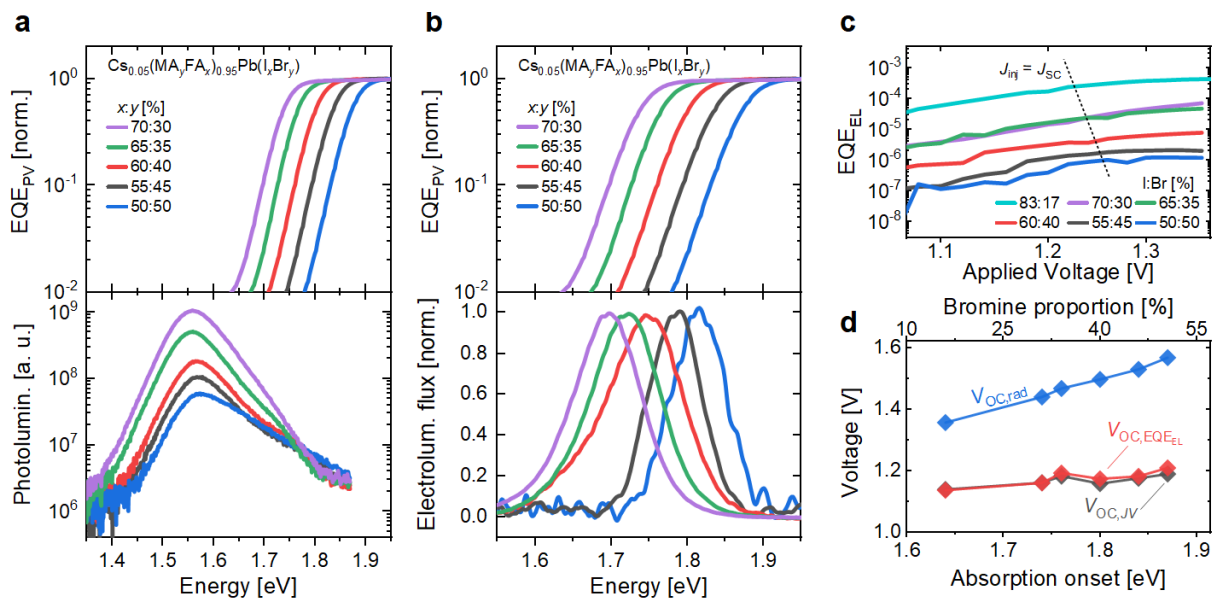


Figure 2. a, Normalised external quantum efficiency (EQE_{PV}) of the wide bandgap perovskite solar cells for several iodine:bromine (x:y) ratios and steady-state photoluminescence (PL) emission spectra showing the position of the peak is centred at ~ 1.55 eV. **b**, Normalised electroluminescence emission spectra showing that the peak emission follows that the bandgap of the different perovskite compositions. **c**, Electroluminescence quantum efficiency (EQE_{EL}) as a function of applied voltage for the selected compositions. The dashed line intersects with the EL curves when the injected current equals short-circuit current density (1 Sun). **d**, The open circuit voltage calculated by means of equation (2) in comparison to the value obtained from the JV-scan.

In order to correlate the observed V_{OC} losses in the wide bandgap cells with the efficiency of radiative recombination, we measured in the next step the external electroluminescence quantum efficiency (EQE_{EL}) as a function of the applied voltage as shown in **Figure 2c**, while **Supplementary Figure S4b** shows the EQE_{EL} as a function of injected current. Under conditions similar to open-circuit under 1-sun illumination (injected current density equals J_{SC}), the EQE_{EL} values monotonically decrease as the bromine proportion (and hence the bandgap) increases. That means that the more the bromine

content, the less the radiative efficiency. The losses in V_{OC} can be quantified starting from the definition of EQE_{EL} as follows

$$EQE_{EL} = \frac{J_{rad}}{J_{R,tot}} = \frac{J_{rad}}{J_{rad} + J_{non-rad}}, \quad (\text{eq. 1})$$

where J_{rad} , $J_{non-rad}$ and $J_{R,tot}$ are the radiative, non-radiative and total recombination current density at a finite QFLS, respectively. Here, $J_{R,tot}$ also corresponds to the total injected current density in EL. Now, from Rau's reciprocity relation⁴¹, it is known that

$$V_{OC} = V_{OC,rad} + \frac{k_B T}{q} \ln(EQE_{EL}) \quad (\text{eq. 2})$$

where k_B the Boltzmann constant, T the temperature, q the elementary charge and $V_{OC,rad}$ is the V_{OC} in the radiative limit given by $V_{OC,rad} = \frac{k_B T}{q} \ln\left(\frac{J_{SC}}{J_{0,rad}}\right)$. Here, $J_{0,rad}$ is the radiative recombination current in the dark. The $V_{OC,rad}$ and the V_{OC} calculated from the EQE_{EL} are shown in the **Figure 2d** along with the measured V_{OC} from the JV -curves. This shows that the V_{OC} losses increase for cells with more content of bromine, i.e. with increasing bandgap. The good agreement between the V_{OC} from the JV scan and the calculated V_{OC} from **Equation 2** further demonstrates that the V_{OC} penalty is due to the low radiative efficiency of the mixed halide phase. Thereby these results demonstrate that the segregated iodide-rich domains and the red-shifted emission are not directly responsible for the losses in V_{OC} .

Having experimentally confirmed that the EQE_{EL} of the mixed phase is comparatively low, in the next step, we aim to understand the reason for this observation. In order to assess the radiative efficiency of the different partial cell stacks comprising the cells, we performed again PL measurements, but this time on fresh samples that have never been exposed to light before. We also illuminated the samples for a very short time ($\sim 1s$) only, before recording the data, hoping to assess the impact of interfacial and bulk recombination on the radiative efficiency prior to significant phase segregation. The results are shown below in **Figure 3**, whilst **Supplementary Figure S5** shows the PL of all stack layers after constant illumination for several minutes, i.e. the impact of phase segregation in these different stack layers. Whereas **Supplementary Figure S5** suggests that C_{60} may partially halt the phase segregation in the absence of the HTL, we aim to analyse the initial measurement of the emission prior to significant segregation that masks the emission from the mixed halide phase. Only this allows to assess the quality of the individual cell components (bulk and transport layers) as previously demonstrated.^{34,35,42} Importantly, similar to the EQE_{EL} , after such a short illumination, the PL originates mainly from the mixed halide phase. At this point it is important to note, that in order to correlate the PL to the QFLS in the film or cell, one needs to analyse the emission of the mixed halide phase, as only this emission is related to the absorption via the principles of detailed balance. Interestingly, **Figure 3** shows that the neat material on glass exhibits by far the highest PLQY while both transport layer cause considerable losses for all perovskite compositions. However, also the PLQY of the neat perovskite drops slightly when going from 1.63 eV to 1.88 eV. We note, that the steady-state PLQY (measured under open-circuit conditions) is given by the ratio of the radiative recombination current to the sum of radiative and non-radiative recombination currents (i.e. in analogy to the EQE_{EL}), i.e. $PLQY = J_{rad}/(J_{rad} + J_{non-rad})$. Therefore, the reduction in PLQY from the neat perovskite to the perovskite/transport layer stacks for a particular perovskite composition, is inversely proportional to the increase of the non-radiative recombination current. Consequently, for all samples, the recombination at the interfaces clearly dominates the overall loss. However, there are distinct

differences among the different perovskite compositions, that is the reduction in the radiative efficiency from low to high bandgap is much more pronounced for the HTL/perovskite stacks. Therefore, while the electron transport layer dominates the recombination in the 83:17, 76:24 and 70:30 perovskite cells, in the higher gap ones, both transport layers limit the PLQY of the *pin*-stack (and complete cell) approximately equally. This results in a significant reduction of the radiative efficiency with respect to the PLQY of the *pin*-stack of the 83:17 composition ($\sim 1.5 \times 10^{-4}$). For example, in the case of the 50:50 triple cation perovskite, the emission from both the HTL/perovskite and perovskite/ETL stack, drops to 2×10^{-5} , whereas the emission of the *pin*-stack is even lower $\sim 7.5 \times 10^{-6}$ (at the same photon energy). As shown in **Supplementary Figure S6**, this is still several times higher than the EQE_{EL} for this particular stack ($\sim 1 \times 10^{-6}$). This mismatch indicates the presence of small energetic offsets between the perovskite and the transport layers for majority carriers, although the difference between the internal QFLS (corresponding to the PLQY) and the V_{OC} (from the EQE_{EL}) is not large (≈ 50 meV).^{36,43} The fact that the HTL interface causes a more rapid decrease in the PLQY would indicate that this offset is mainly at the HTL interface, however the low PLQY could be also related to an increasingly high defect density at this interface. The hypothesis of an energy offset at the *p*-interface would be consistent with literature where an increasing amount of Br has been found to correlate with a larger ionization potential, although triple cation perovskites as studied here have not been directly analysed in these works.^{44–46} To test the energy offset at the *p*-interface, we measured the UPS on ITO/HTL and ITO/HTL/perovskite layer stacks for different perovskite compositions.^{47,48} Surprisingly, under illumination, we found no significant energy offset between the valence band of PTAA:PFN-Br and the perovskite as shown in **Supplementary Figure S7**. This suggests that the defect density at the HTL is the more critical factor in lowering the PLQY although this conclusion will require further studies in the future.

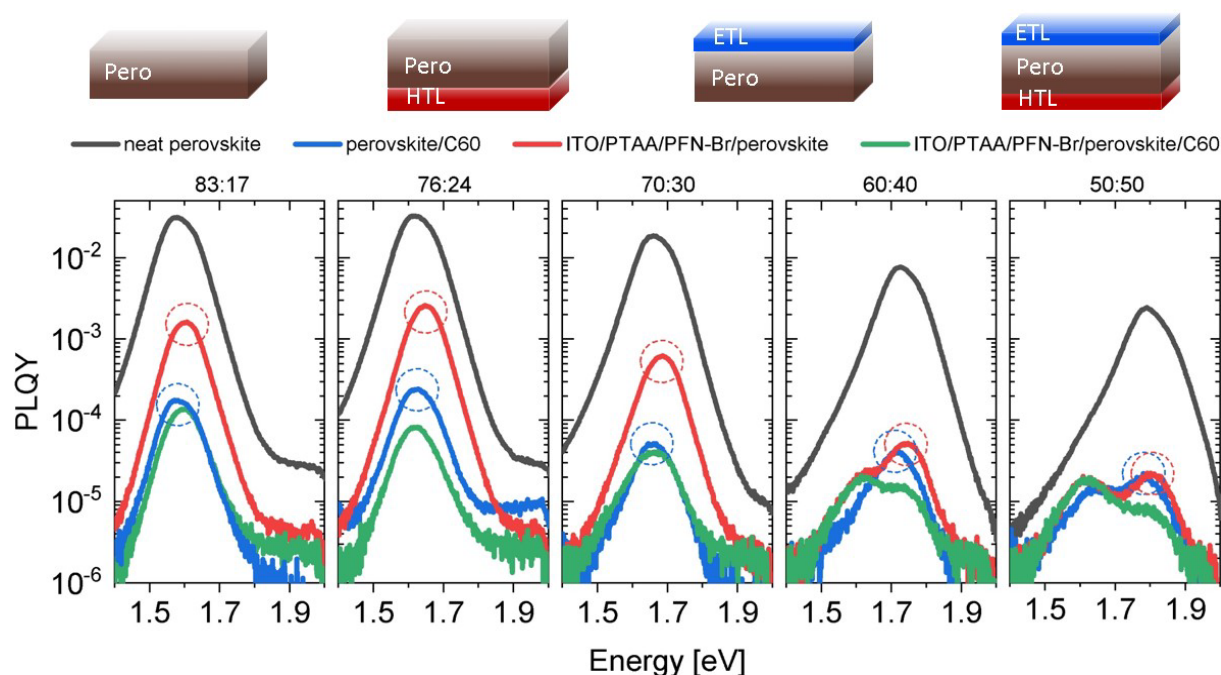


Figure 3. Photoluminescence quantum yield (PLQY) on partial solar cell stacks for five perovskite compositions highlighting the strong reduction in the PL emission from the perovskite, in particular in the presence of the transport layers, upon increasing the bromine content. The emission flux on the *y*-axis has been scaled to represent the photoluminescence quantum yield at the peak position. The upper label stands for the proportion (in molar %) of FAPbI_3 (*x*) and MAPbBr_3 (*y*) in the triple cation perovskite $\text{Cs}_{0.05}(\text{FA}_x\text{MA}_y)_{0.95}\text{Pb}(\text{I}_x\text{Br}_y)_3$.

Finally, in order to improve the performance of these cells, we aimed to suppress the recombination at the n -interface by including lithium fluoride (LiF) as an effective interlayer between the perovskite and the C_{60} . As previously shown,⁴⁹ LiF can significantly reduce the decisive interfacial recombination losses, although its working mechanism was never fully clarified, despite some attempts.⁵⁰ As shown in **Figure 4b**, for those cells whose bandgap is below 1.74 eV, the performance is improved by the inclusion of this interlayer. Particularly for cells with a bandgap of 1.69 eV, there is an improvement from 18.6 to 20.1 % in PCE due a combination of FF and V_{oc} gains. The average performance parameters of cells with LiF are shown in **Supplementary Figure S8** while **Supplementary Figure S9** shows hysteresis scans of the JV curves. In order to further elucidate the working mechanism of LiF, we performed ultraviolet photoelectron spectroscopy (UPS) measurements on perovskite films with and without LiF and C_{60} , as shown in **Supplementary Figure S10**. Strikingly, LiF induces a significant decrease in the perovskite work function indicating the presence of a surface dipole that repels holes from the C_{60} layer. This is consistent with the identical binding energies of the iodine core levels as shown in **Supplementary Figure S10**. Interestingly, however, the passivation does not work anymore for even wider bandgap cells (≥ 1.75 eV). This completes the above findings, which demonstrate that the HTL interface becomes strongly limiting at a bandgap 1.8 eV corresponding to a perovskite composition of 60:40. Therefore, in order to improve the performance of these cells further, the recombination at the HTL must be simultaneously improved with the n -interface in the future.

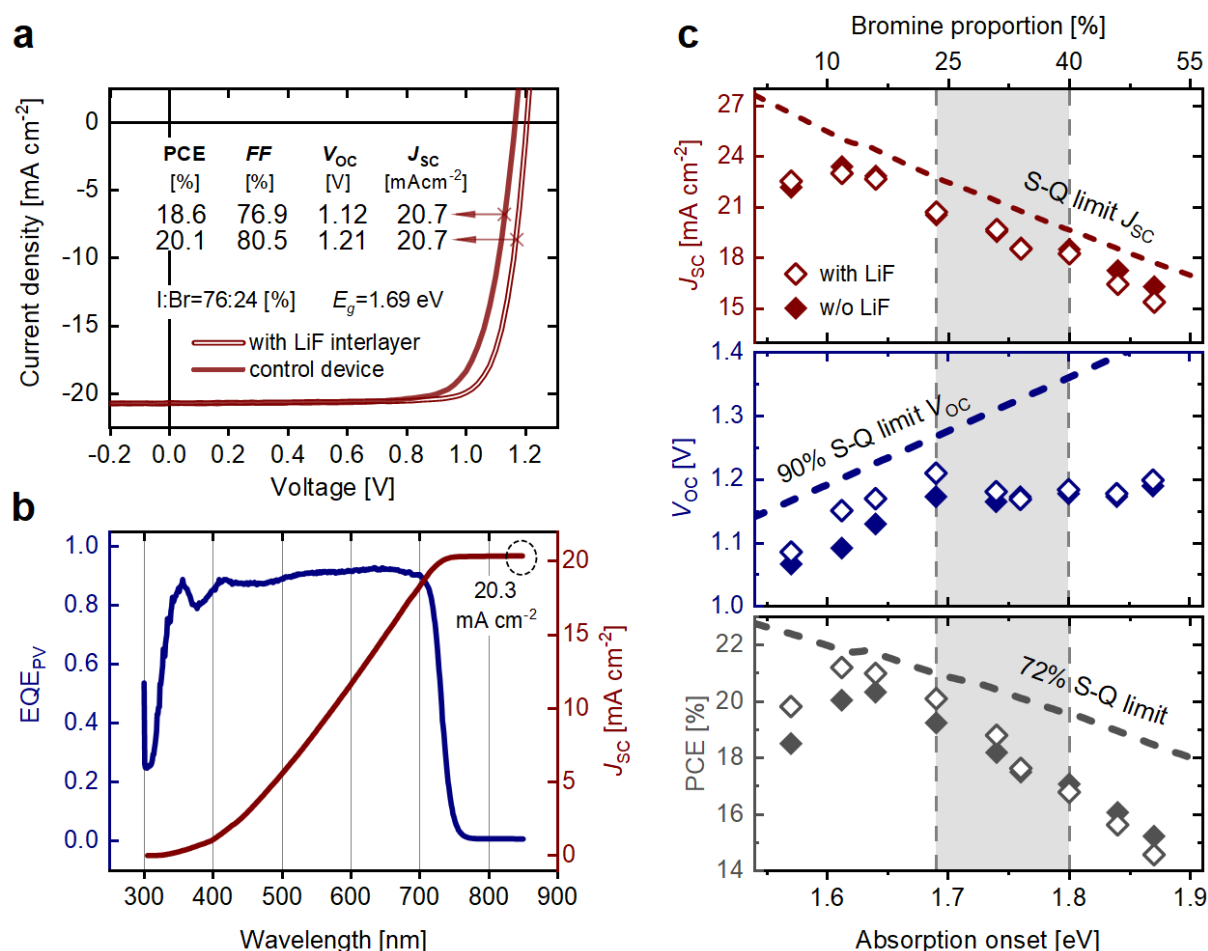


Figure 4. **a**, Performance improvement upon LiF addition in triple cation perovskite cells with a bandgap of 1.69 eV. **b**, External quantum efficiency of the LiF-containing cell shown in panel a. **c**, Summary of the impact of LiF on the photovoltaic performance parameters for perovskite cells with varying bandgap (the best performing cells are shown for each composition). The grey area highlights the targeted compositions intended for silicon-perovskite and all-perovskite tandem cells.

Interestingly, while LiF significantly improves the performance of cells up to 1.74 eV, at even higher bandgaps, the performance cannot be further improved due to the limitations imposed by the HTL.

Conclusions

In this work, we have performed a thorough investigation of open-circuit voltage losses in wide bandgap triple perovskite solar cells that are relevant for tandem solar cells applications. In line with literature, also in this type of perovskite solar cells, we find a remarkable saturation of the open-circuit voltage when increasing the perovskite bandgap beyond the optimum of 1.63 eV. Aiming to improve the performance, we introduced an ultrathin lithium fluoride (LiF) layer between the perovskite and C₆₀ which was found to induce a significant reduction (~0.65 eV) of the perovskite work function. This improved the performance to 20% (through an increase in the V_{OC} and FF) for a perovskites with a bandgap of up to 1.69 eV, although LiF did not improve the performance of cells with a gap larger than 1.75 eV. To understand the saturation of the V_{OC} , we recorded photoluminescence spectra on previously illuminated cells. This revealed an emission peak being centred at 1.55 eV (at a Br ratio >30%), consistent with emission of iodide rich domains, thereby confirming that the samples were already phase-segregated. We then correlated the PL spectra with the EL emission and found a surprising difference between these two measurements. In fact, the EL spectra followed the expected emission from the mixed phase, which allowed us to directly access the non-radiative recombination losses in the mixed halide perovskite phase that governs the light absorption. By measuring the EQE_{EL} we could experimentally confirm that the mixed perovskite composition explains the V_{OC} of the cells and therefore the V_{OC} losses with increasing Br concentration. Additional measurements on partial perovskite solar cells that were never exposed to light uncovered significant non-radiative recombination at both interfaces prior to significant halide segregation that would mask the emission from the mixed phase. This highlights that the emission from iodide-rich domains is not the dominant factor in determining the V_{OC} of the cells but that it is rather the high interfacial defect density in the mixed halide phase and partially improper energy alignment that causes the losses. The findings of this work suggest that interfacial engineering, in particular the *p*-interface, will enable higher open-circuit voltages in wide-gap perovskites (≥ 1.75 eV) in the near future.

References

- (1) Steirer, K. X.; Schulz, P.; Teeter, G.; Stevanovic, V.; Yang, M.; Zhu, K.; Berry, J. J. Defect Tolerance in Methylammonium Lead Triiodide Perovskite. *ACS Energy Lett.* **2016**, *1*, 360–366.
- (2) Shi, D.; Adinolfi, V.; Comin, R.; Yuan, M.; Alarousu, E.; Buin, A.; Chen, Y.; Hoogland, S.; Rothenberger, A.; Katsiev, K.; Losovyj, Y.; Zhang, X.; Dowben, P. A.; Mohammed, O. F.; Sargent, E. H.; Bakr, O. M. Low Trap-State Density and Long Carrier Diffusion in Organolead Trihalide Perovskite Single Crystals. *Science* **2015**, *347*, 519–522.
- (3) Wang, L.; Yuan, G. D.; Duan, R. F.; Huang, F.; Wei, T. B.; Liu, Z. Q.; Wang, J. X.; Li, J. M. Tunable Bandgap in Hybrid Perovskite CH₃NH₃Pb(Br_{3-y}X_y) Single Crystals and Photodetector Applications. *AIP Adv.* **2016**, *6*, 45115.
- (4) Dou, L.; Yang, Y. M.; You, J.; Hong, Z.; Chang, W. H.; Li, G.; Yang, Y. Solution-Processed Hybrid Perovskite Photodetectors with High Detectivity. *Nat. Commun.* **2014**, *5*, 1–6.
- (5) Sutherland, B. R.; Sargent, E. H. Perovskite Photonic Sources. *Nat. Photon.* **2016**, *10*, 295–302.
- (6) Cho, H.; Jeong, S.-H.; Park, M.-H.; Kim, Y.-H.; Wolf, C.; Lee, C.-L.; Heo, J. H.; Sadhanala, A.; Myoung, N.; Yoo, S.; Im, S. H.; Friend, R. H.; Lee, T.-W. Overcoming the Electroluminescence

- Efficiency Limitations of Perovskite Light-Emitting Diodes. *Science* **2015**, *350*, 1222 LP – 1225.
- (7) Eperon, G. E.; Stranks, S. D.; Menelaou, C.; Johnston, M. B.; Herz, L. M.; Snaith, H. J. Formamidinium Lead Trihalide: A Broadly Tunable Perovskite for Efficient Planar Heterojunction Solar Cells. *Energy Environ. Sci.* **2014**, *7*, 982.
 - (8) Park, N.-G.; Grätzel, M.; Miyasaka, T.; Zhu, K.; Emery, K. Towards Stable and Commercially Available Perovskite Solar Cells. *Nat. Energy* **2016**, *1*, 16152.
 - (9) Kirchartz, T. High Open-Circuit Voltages in Lead-Halide Perovskite Solar Cells: Experiment, Theory and Open Questions. *Philos. Trans. R. Soc. A Math. Phys. Eng. Sci.* **2019**, *377*, 20180286.
 - (10) Nations, U. 17 Goals to Transform Our World: Ensure access to affordable, reliable, sustainable and modern energy.
 - (11) Chen, C.-C.; Bae, S.-H.; Chang, W.-H.; Hong, Z.; Li, G.; Chen, Q.; Zhou, H.; Yang, Y. Perovskite/Polymer Monolithic Hybrid Tandem Solar Cells Utilizing a Low-Temperature, Full Solution Process. *Mater. Horiz.* **2015**, *2*, 203–211.
 - (12) Forgács, D.; Gil-escrig, L.; Pérez-del-rey, D.; Momblona, C.; Werner, J.; Niesen, B.; Ballif, C.; Sessolo, M.; Bolink, H. J. Efficient Monolithic Perovskite / Perovskite Tandem Solar Cells. **2017**, 1–6.
 - (13) Zhu, X.; Yang, D.; Yang, R.; Yang, B.; Yang, Z.; Ren, X.; Zhang, J.; Niu, J.; Feng, J.; Liu, S. (Frank). Superior Stability for Perovskite Solar Cells with 20% Efficiency Using Vacuum Co-Evaporation. *Nanoscale* **2017**, *9*, 12316–12323.
 - (14) Zhao, Q.; Hazarika, A.; Chen, X.; Harvey, S. P.; Larson, B. W.; Teeter, G. R.; Liu, J.; Song, T.; Xiao, C.; Shaw, L.; Zhang, M.; Li, G.; Beard, M. C.; Luther, J. M. High Efficiency Perovskite Quantum Dot Solar Cells with Charge Separating Heterostructure. *Nat. Commun.* **2019**, *10*, 2842.
 - (15) Zhang, Y.; Gu, M.; Li, N.; Xu, Y.; Ling, X.; Wang, Y.; Zhou, S.; Li, F.; Yang, F.; Ji, K.; Yuan, J.; Ma, W. Realizing Solution-Processed Monolithic PbS QDs/Perovskite Tandem Solar Cells with High UV Stability. *J. Mater. Chem. A* **2018**, *6*, 24693–24701.
 - (16) Gao, K.; Zhu, Z.; Xu, B.; Jo, S. B.; Kan, Y.; Peng, X.; Jen, A. K.-Y. Highly Efficient Porphyrin-Based OPV/Perovskite Hybrid Solar Cells with Extended Photoresponse and High Fill Factor. *Adv. Mater.* **2017**, *29*, 1703980.
 - (17) Liu, J.; Lu, S.; Zhu, L.; Li, X.; Choy, W. C. H. Perovskite–Organic Hybrid Tandem Solar Cells Using a Nanostructured Perovskite Layer as the Light Window and a PFN/Doped-MoO₃/MoO₃ Multilayer as the Interconnecting Layer. *Nanoscale* **2016**, *8*, 3638–3646.
 - (18) Eperon, G. E.; Leijtens, T.; Bush, K. A.; Prasanna, R.; Green, T.; Wang, J. T.; Mcmeekin, D. P.; Volonakis, G.; Milot, R. L.; May, R.; Palmstrom, A.; Slotcavage, D. J.; Belisle, R. A.; Patel, J. B.; Parrott, E. S.; Sutton, R. J.; Ma, W.; Moghadam, F.; Conings, B.; Babayigit, A.; Boyen, H.; Bent, S.; McGehee, M. D.; Snaith, H. J. Perovskite-Perovskite Tandem Photovoltaics with Optimized Band Gaps. **2016**, *354*, 861–866.
 - (19) Lin, R.; Xiao, K.; Qin, Z.; Han, Q.; Zhang, C.; Wei, M.; Saidaminov, M. I.; Gao, Y.; Xu, J.; Xiao, M.; Li, A.; Zhu, J.; Sargent, E. H.; Tan, H. Monolithic All-Perovskite Tandem Solar Cells with 24.8% Efficiency Exploiting Comproportionation to Suppress Sn(II) Oxidation in Precursor Ink. *Nat. Energy* **2019**, *4*, 864–873.
 - (20) Köhnen, E.; Jošt, M.; Morales-Vilches, A. B.; Tockhorn, P.; Al-Ashouri, A.; Macco, B.; Kegelmann, L.; Korte, L.; Rech, B.; Schlattmann, R.; Stannowski, B.; Albrecht, S. Highly Efficient Monolithic Perovskite Silicon Tandem Solar Cells: Analyzing the Influence of Current Mismatch on Device Performance. *Sustain. Energy Fuels* **2019**, *3*, 1995–2005.

- (21) Hou, Y.; Aydin, E.; De Bastiani, M.; Xiao, C.; Isikgor, F. H.; Xue, D.-J.; Chen, B.; Chen, H.; Bahrami, B.; Chowdhury, A. H.; Johnston, A.; Baek, S.-W.; Huang, Z.; Wei, M.; Dong, Y.; Troughton, J.; Jalmood, R.; Mirabelli, A. J.; Allen, T. G.; Van Kerschaver, E.; Saidaminov, M. I.; Baran, D.; Qiao, Q.; Zhu, K.; De Wolf, S.; Sargent, E. H. Efficient Tandem Solar Cells with Solution-Processed Perovskite on Textured Crystalline Silicon. *Science* **2020**, *367*, 1135 LP – 1140.
- (22) Bush, K. A.; Palmstrom, A. F.; Yu, Z. J.; Boccard, M.; Cheacharoen, R.; Mailoa, J. P.; McMeekin, D. P.; Hoyer, R. L. Z.; Bailie, C. D.; Leijtens, T.; Peters, I. M.; Minichetti, M. C.; Rolston, N.; Prasanna, R.; Sofia, S.; Harwood, D.; Ma, W.; Moghadam, F.; Snaith, H. J.; Buonassisi, T.; Holman, Z. C.; Bent, S. F.; McGehee, M. D. 23.6%-Efficient Monolithic Perovskite/Silicon Tandem Solar Cells With Improved Stability. *Nat. Energy* **2017**, *2*, 17009.
- (23) Jošt, M.; Bertram, T.; Koushik, D.; Marquez, J. A.; Verheijen, M. A.; Heinemann, M. D.; Köhnen, E.; Al-Ashouri, A.; Braunger, S.; Lang, F.; Rech, B.; Unold, T.; Creatore, M.; Lauermaun, I.; Kaufmann, C. A.; Schlatmann, R.; Albrecht, S. 21.6%-Efficient Monolithic Perovskite/Cu(In,Ga)Se₂ Tandem Solar Cells with Thin Conformal Hole Transport Layers for Integration on Rough Bottom Cell Surfaces. *ACS Energy Lett.* **2019**, *4*, 583–590.
- (24) Paetzold, U. W.; Jaysankar, M.; Gehlhaar, R.; Ahlswede, E.; Paetel, S.; Qiu, W.; Bastos, J.; Rakocevic, L.; Richards, B. S.; Aernouts, T.; Powalla, M.; Poortmans, J. Scalable Perovskite/CIGS Thin-Film Solar Module with Power Conversion Efficiency of 17.8%. *J. Mater. Chem. A* **2017**, *5*, 9897–9906.
- (25) Eperon, G. E.; Hörantner, M. T.; Snaith, H. J. Metal Halide Perovskite Tandem and Multiple-Junction Photovoltaics. *Nat. Rev. Chem.* **2017**, *1*, 95.
- (26) Lal, N. N.; Dkhissi, Y.; Li, W.; Hou, Q.; Cheng, Y.-B.; Bach, U. Perovskite Tandem Solar Cells. *Adv. Energy Mater.* **2017**, *7*, 1602761.
- (27) Todorov, T.; Gershon, T.; Gunawan, O.; Sturdevant, C.; Guha, S. Perovskite-Kesterite Monolithic Tandem Solar Cells with High Open-Circuit Voltage. *Appl. Phys. Lett.* **2014**, *105*, 173902.
- (28) Unger, E. L.; Kegelmann, L.; Suchan, K.; Sörell, D.; Korte, L.; Albrecht, S. Roadmap and Roadblocks for the Band Gap Tunability of Metal Halide Perovskites. *J. Mater. Chem. A* **2017**, *5*, 11401–11409.
- (29) Noh, J. H.; Im, S. H.; Heo, J. H.; Mandal, T. N.; Seok, S. I. Chemical Management for Colorful, Efficient, and Stable Inorganic–Organic Hybrid Nanostructured Solar Cells. *Nano Lett.* **2013**, *13*, 1764.
- (30) Mahesh, S.; Ball, J. M.; Oliver, R. D. J.; McMeekin, D. P.; Nayak, P. K.; Johnston, M. B.; Snaith, H. J. Revealing the Origin of Voltage Loss in Mixed-Halide Perovskite Solar Cells. *Energy Environ. Sci.* **2020**, *13*, 258–267.
- (31) Kulkarni, S. A.; Baikie, T.; Boix, P. P.; Yantara, N.; Mathews, N.; Mhaisalkar, S. Band-Gap Tuning of Lead Halide Perovskites Using a Sequential Deposition Process. *J. Mater. Chem. A* **2014**, *2*, 9221–9225.
- (32) Hoke, E. T.; Slotcavage, D. J.; Dohner, E. R.; Bowring, A. R.; Karunadasa, H. I.; McGehee, M. D. Reversible Photo-Induced Trap Formation in Mixed-Halide Hybrid Perovskites for Photovoltaics. *Chem. Sci.* **2015**, *6*, 613.
- (33) Slotcavage, D. J.; Karunadasa, H. I.; McGehee, M. D. Light-Induced Phase Segregation in Halide-Perovskite Absorbers. *ACS Energy Lett.* **2016**, *1*, 1199.
- (34) Stolterfoht, M.; Wolff, C. M.; Márquez, J. A.; Zhang, S.; Hages, C. J.; Rothhardt, D.; Albrecht, S.; Burn, P. L.; Meredith, P.; Unold, T.; Neher, D. Visualization and Suppression of Interfacial Recombination for High-Efficiency Large-Area Pin Perovskite Solar Cells. *Nat. Energy* **2018**, *3*,

847–854.

- (35) Wolff, C. M.; Caprioglio, P.; Stolterfoht, M.; Neher, D. Nonradiative Recombination in Perovskite Solar Cells : The Role of Interfaces. *2019*, 1902762.
- (36) Stolterfoht, M.; Caprioglio, P.; Wolff, C. M.; Márquez, J. A.; Nordmann, J.; Zhang, S.; Rothhardt, D.; Hörmann, U.; Amir, Y.; Redinger, A.; Kegelmann, L.; Zu, F.; Albrecht, S.; Koch, N.; Kirchartz, T.; Saliba, M.; Unold, T.; Neher, D. The Impact of Energy Alignment and Interfacial Recombination on the Internal and External Open-Circuit Voltage of Perovskite Solar Cells. *Energy Environ. Sci.* **2019**, 12, 2778–2788.
- (37) Gharibzadeh, S.; Abdollahi Nejang, B.; Jakoby, M.; Abzieher, T.; Hauschild, D.; Moghadamzadeh, S.; Schwenzer, J. A.; Brenner, P.; Schmager, R.; Haghighirad, A. A.; Weinhardt, L.; Lemmer, U.; Richards, B. S.; Howard, I. A.; Paetzold, U. W. Record Open-Circuit Voltage Wide-Bandgap Perovskite Solar Cells Utilizing 2D/3D Perovskite Heterostructure. *Adv. Energy Mater.* **2019**, 9.
- (38) Brennan, M. C.; Draguta, S.; Kamat, P. V.; Kuno, M. Light-Induced Anion Phase Segregation in Mixed Halide Perovskites. *ACS Energy Lett.* **2018**, 3, 204.
- (39) Knight, A. J.; Patel, J. B.; Snaith, H. J.; Johnston, M. B.; Herz, L. M. Trap States, Electric Fields, and Phase Segregation in Mixed-Halide Perovskite Photovoltaic Devices. *Adv. Energy Mater.* **2020**, n/a, 1903488.
- (40) Rau, U.; Paetzold, U. W.; Kirchartz, T. Thermodynamics of Light Management in Photovoltaic Devices. *Phys. Rev. B* **2014**, 90, 35211.
- (41) Rau, U. Reciprocity Relation between Photovoltaic Quantum Efficiency and Electroluminescent Emission of Solar Cells. *Phys. Rev. B* **2007**, 76, 085303.
- (42) Stolterfoht, M.; Grischek, M.; Caprioglio, P.; Wolff, C. M.; Gutierrez-Partida, E.; Peña-Camargo, F.; Rothhardt, D.; Zhang, S.; Raoufi, M.; Wolansky, J.; Abdi-Jalebi, M.; Stranks, S. D.; Albrecht, S.; Kirchartz, T.; Neher, D. How To Quantify the Efficiency Potential of Neat Perovskite Films: Perovskite Semiconductors with an Implied Efficiency Exceeding 28%. *Adv. Mater.* **2020**, 32, 2000080.
- (43) Caprioglio, P.; Stolterfoht, M.; Wolff, C. M.; Unold, T.; Rech, B.; Albrecht, S.; Neher, D. On the Relation between the Open-Circuit Voltage and Quasi-Fermi Level Splitting in Efficient Perovskite Solar Cells. *Adv. Energy Mater.* **2019**, 9, 1901631.
- (44) Li, C.; Wei, J.; Sato, M.; Koike, H.; Xie, Z. Z.; Li, Y. Q.; Kanai, K.; Kera, S.; Ueno, N.; Tang, J. X. Halide-Substituted Electronic Properties of Organometal Halide Perovskite Films: Direct and Inverse Photoemission Studies. *ACS Appl. Mater. Interfaces* **2016**, 8, 11526–11531.
- (45) Zhou, X.; Ye, W.; Li, X.; Zheng, W.; Lin, R.; Huang, F.; Zhong, D. Band Alignment of MAPb(I 1– x Br x) 3 Thin Films by Vacuum Deposition. *Appl. Phys. Lett.* **2016**, 109, 233906.
- (46) Tao, S.; Schmidt, I.; Brocks, G.; Jiang, J.; Tranca, I.; Meerholz, K.; Olthof, S. Absolute Energy Level Positions in Tin- and Lead-Based Halide Perovskites. *Nat. Commun.* **2019**, 10, 1–10.
- (47) Zu, F.; Wolff, C. M.; Ralaiarisoa, M.; Amsalem, P.; Neher, D.; Koch, N. Unraveling the Electronic Properties of Lead Halide Perovskites with Surface Photovoltage in Photoemission Studies. *ACS Appl. Mater. Interfaces* **2019**, 11, 21578–21583.
- (48) Zu, F. S.; Amsalem, P.; Salzmann, I.; Wang, R. Bin; Ralaiarisoa, M.; Kowarik, S.; Duhm, S.; Koch, N. Impact of White Light Illumination on the Electronic and Chemical Structures of Mixed Halide and Single Crystal Perovskites. *Adv. Opt. Mater.* **2017**, 5.
- (49) Limmer, D. T.; Ginsberg, N. S. Photoinduced Phase Separation in the Lead Halides Is a Polaronic Effect. 2020.

- (50) Shao, S.; Liu, J.; Fang, H.; Qiu, L.; ten Brink, G. H.; Hummelen, J. C.; Koster, L. J. A.; Loi, M. A. Efficient Perovskite Solar Cells over a Broad Temperature Window: The Role of the Charge Carrier Extraction. *Adv. Energy Mater.* **2017**, *7*, 1701305.

Halide segregation versus interfacial recombination in bromide-rich wide-gap perovskite solar cells

Francisco Peña-Camargo¹, Pietro Caprioglio^{1,2}, Fengshuo Zu^{3,4}, Emilio Gutierrez-Partida¹, Christian M. Wolff¹, Kai Brinkmann⁵, Steve Albrecht², Thomas Riedl⁵, Norbert Koch^{3,4}, Dieter Neher¹, Martin Stolterfoht^{1,*}

¹Institute of Physics and Astronomy, University of Potsdam, Karl-Liebknecht-Str. 24-25, D-14476 Potsdam-Golm, Germany.

²Young Investigator Group Perovskite Tandem Solar Cells, Helmholtz-Zentrum Berlin für Materialien und Energie GmbH, Kekuléstraße 5, 12489 Berlin, Germany

³Helmholtz-Zentrum Berlin für Materialien und Energie GmbH, 12489 Berlin, Germany

⁴Institut für Physik & IRIS Adlershof, Humboldt-Universität zu Berlin, 12489 Berlin, Germany

⁵Institute of Electronic Devices, University of Wuppertal, Rainer-Gruenter-Str 21, 42119 Wuppertal, Germany

email: stolterf@uni-potsdam.de

Supplementary Methods

Absolute Photoluminescence Measurements: Excitation for the PL imaging measurements was performed with a 520 nm CW laser (Insaneware) through an optical fibre into an integrating sphere. The intensity of the laser was adjusted to a 1 sun equivalent intensity by illuminating a 1 cm²-size perovskite solar cell under short-circuit and matching the current density to the J_{SC} under the sun simulator (e.g. ~ 22.0 mA/cm² at 100 mW/cm², or 1.375×10^{21} photons m⁻²s⁻¹ for a 83-17 triple cation perovskite cell). A second optical fiber was used from the output of the integrating sphere to an Andor SR393i-B spectrometer equipped with a silicon CCD camera (DU420A-BR-DD, iDus). The system was calibrated by using a halogen lamp with known spectral irradiance, which was shone into to integrating sphere. A spectral correction factor was established to match the spectral output of the detector to the calibrated spectral irradiance of the lamp. The spectral photon density was obtained from the corrected detector signal (spectral irradiance) by division through the photon energy (hf), and the photon numbers of the excitation and emission were obtained from numerical integration using Matlab. In a last step, three fluorescent test samples with high specified PLQY ($\sim 70\%$) supplied from Hamamatsu Photonics where measured where the specified value could be accurately reproduced within a small relative error of less than 5%.

Device Fabrication of *pin*-type cells: Substrates and HTL: Pre-patterned 2.5x2.5 cm² 15 Ω /sq. ITO substrates (Automatic Research, Germany) were cleaned with acetone, 3% Hellmanex solution, DI-water and iso-propanol, by sonication for 10 min in each solution. After a microwave plasma treatment (3 min, 200 W), the samples were transferred to a N₂-filled glovebox. For the *pin*-type cells shown in the main text, a PTAA (Sigma-Aldrich) layer with thickness of 8 nm was spin coated from a 1.5 mg mL⁻¹ PTAA/toluene solution at 6000 rpm for 30 seconds. After 10 min annealing on a hotplate at 100 °C, the films were cooled down to room temperature and a 60 μ L solution of PFN-Br (1-Material, 0.5 mg/mL in methanol) was deposited onto PTAA while the substrate was being spun at 5000 rpm for 20 s resulting in a film with thickness below the detection limit of our AFM (< 5 nm). No further annealing occurred.

Perovskite solutions: The triple cation perovskite solutions were prepared by mixing two 1.2 M FAPbI₃ and MAPbBr₃ perovskite solutions in DMF:DMSO (4:1 volume ratio, v:v) in a certain ratio of x:y (FAPbI₃:MAPbBr₃, e.g. 83:17) which we call "MAFA" solution. The 1.2 M FAPbI₃ solution was thereby prepared by dissolving FAI (722 mg) and PbI₂ (2130 mg) in 2.8 mL DMF and 0.7 mL DMSO which

contains a 10 molar% excess of PbI_2 . The 1.2 M MAPbBr_3 solution was made by dissolving MABr (470 mg) and PbBr_2 (1696 mg) in 2.8 mL DMF and 0.7 mL DMSO which contains a 10 molar% excess of PbBr_2 . Lastly, 40 μL of a 1.5 CsI solution in DMSO (389 mg CsI in 1 mL DMSO) was mixed with 960 μL of the MAFA solution resulting in a nominal perovskite stoichiometry of $\text{Cs}_{0.05}(\text{FA}_x\text{MA}_y)_{0.95}\text{Pb}(\text{I}_x\text{Br}_y)_3$ respectively.

Perovskite film fabrication: All triple cation perovskite films were deposited by spin-coating at 4500 rpm for 35 s and 10 s after the start of the spinning process, the spinning substrate was washed with 300 μL ethylacetate for approximately 1 s (the anti-solvent was placed in the centre of the film). We note, that by the end of the spinning process the perovskite film turned dark brown. The perovskite film was then annealed at 100 $^\circ\text{C}$ for 1 h on a preheated hotplate where the film turned slightly more dark.

ETL and Top Contact: After annealing, the samples were transferred to an evaporation chamber where fullerene- C_{60} (30 nm), 2,9-Dimethyl-4,7-diphenyl-1,10-phenanthroline BCP (8 nm) and copper (100 nm) were deposited under vacuum ($p = 10^{-7}$ mbar). The overlap of the copper and the ITO electrodes defined the active area of the pixel (6 mm^2).

Current density-voltage characteristics: JV -curves were obtained in a 2-wire source-sense configuration with a Keithley 2400. An Oriel class AAA Xenon lamp-based sun simulator was used for illumination providing approximately 100 mW cm^{-2} of AM1.5G irradiation and the intensity was monitored simultaneously with a Si photodiode. The exact illumination intensity was used for efficiency calculations, and the simulator was calibrated with a KG5 filtered silicon solar cell (certified by Fraunhofer ISE). The obtained short-circuit current density (J_{SC}) is checked by integrating the product of the External Quantum Efficiency and the solar spectrum which matches the obtained J_{SC} within less than 5%. The temperature of the cell was fixed to 25 $^\circ\text{C}$ and a voltage ramp (scan rate) of 67 mV/s was used. JV -curves at different scans speeds and stabilization times are presented in **Supplementary Figure S2**.

Electroluminescence: Absolute EL was measured with a calibrated Si photodetector (Newport) connected to a Keithley 485 pico Ampere meter. The detector (with an active area of $\sim 2 \text{ cm}^2$) was placed directly in front of the device ($< 0.5 \text{ cm}$) and the total photon flux was evaluated considering the emission spectrum of the solar cell and the external quantum efficiency of the detector (around $\approx 86 \%$ in the relevant spectral regime). A forward bias was applied to the cell using a Keithley 2400 source-meter and the injected current was monitored. Measurements were conducted with a home written LabVIEW routine. Typically, the voltage was increased in steps of 20 mV and the current stabilized for typical 1s at each step. No relevant changes in the EQE_{EL} were observed for different stabilization times.

Ultraviolet photoelectron spectroscopy (UPS) measurements were performed at an ultra-high vacuum system (base pressure of 5×10^{-10} mbar) using a monochromatized helium discharge lamp (photon energy of 21.22 eV) and a hemispherical analyzer (SPECS Phoibos 100). The SECO spectra were recorded at a bias of -10 V on the samples to overcome the work function of the analyzer. The valence band onsets were extrapolated on a logarithmic photoemission intensity scale.^{1,2} All spectra were recorded at room temperature and various the excitation photo-fluxes were tested (e.g. varying the UV flux as well as by applying an additional white light), to investigate the surface photovoltage effect as established by our previous report.³

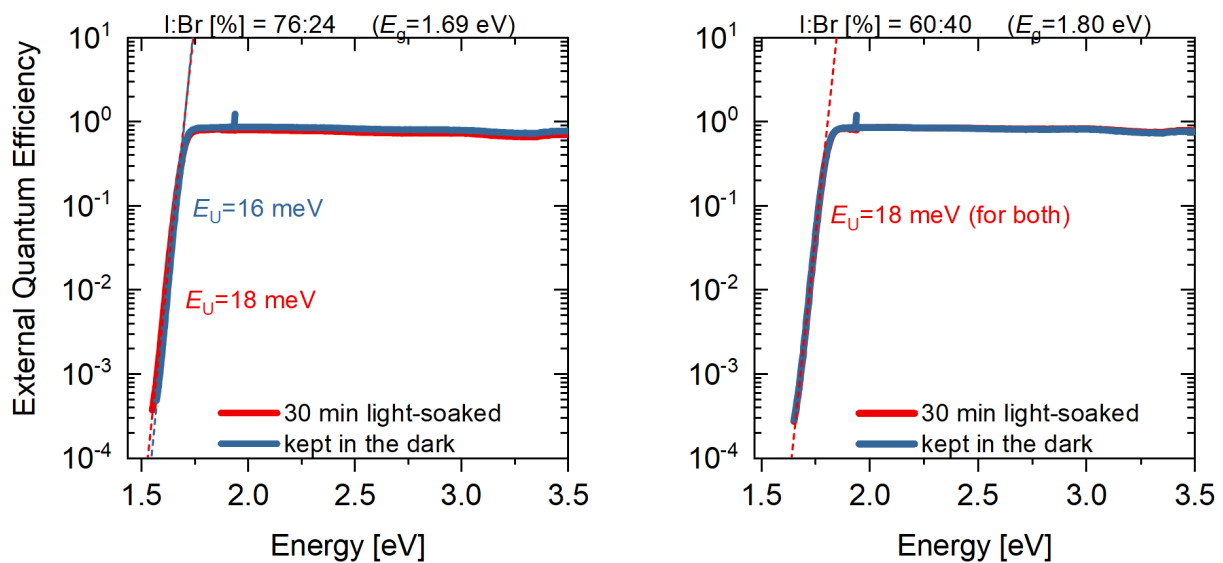
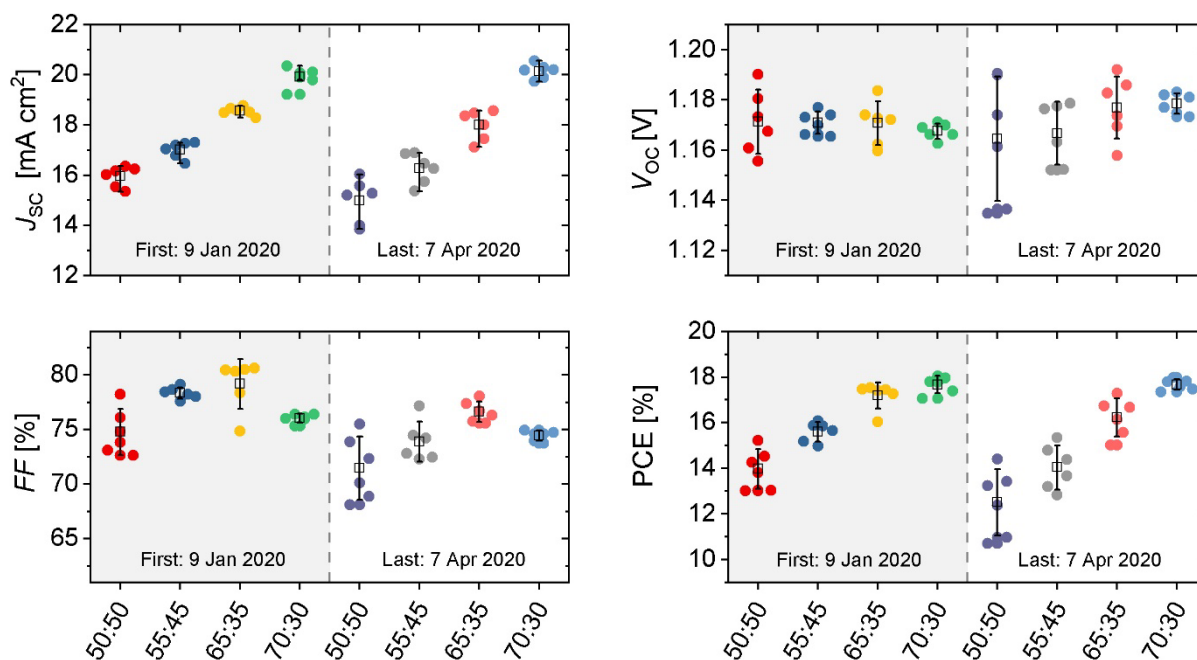
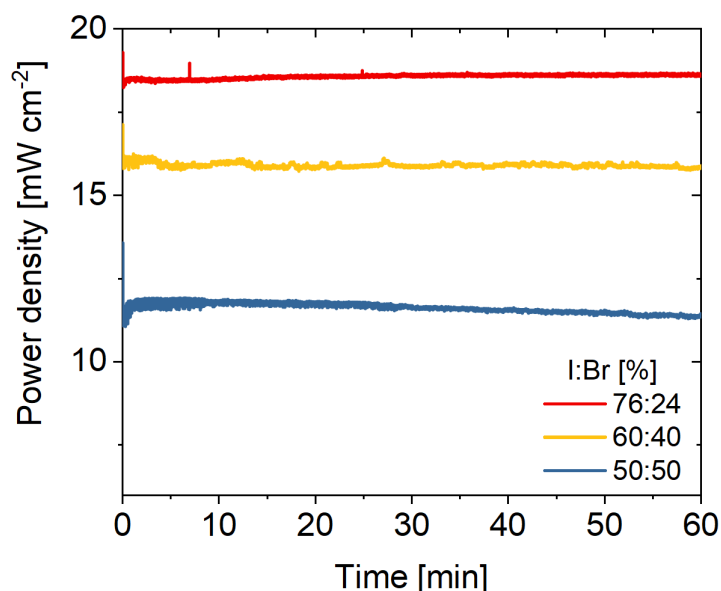


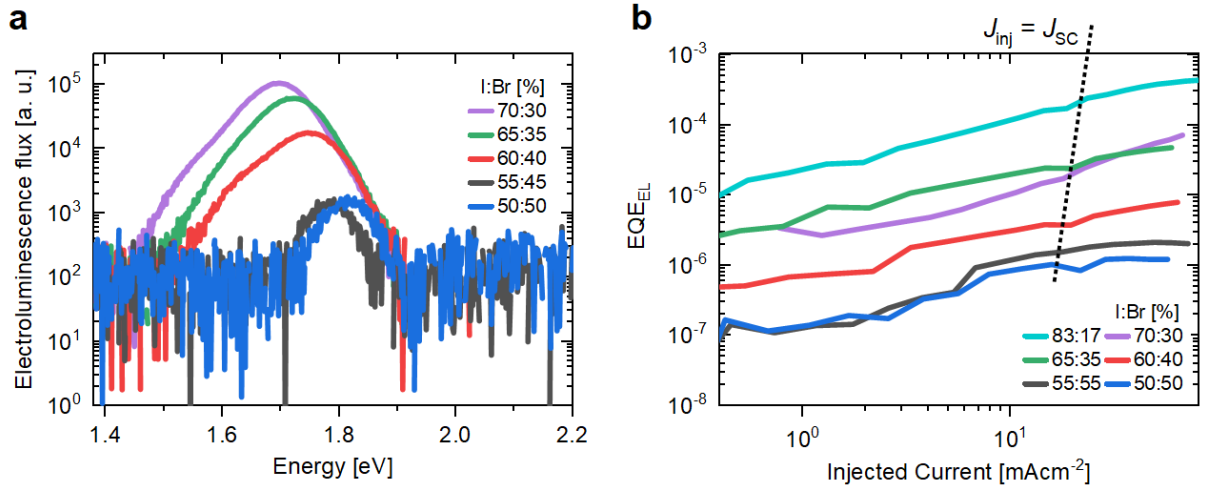
Figure S1. EQE_{PV} curves of cell with three different triple cation compositions $\text{Cs}_{0.05}(\text{MA}_y\text{FA}_x)_{0.95}\text{Pb}(\text{I}_x\text{Br}_y)_3$ where the $x:y=\text{I}:\text{Br}$ [%] ratio is shown on top along with the corresponding bandgap. Note, the measurements were performed on the same cells shown in **Figure 2a** and **2b** after the PL and EL measurements. First, the measurement is taken on the cells which were kept in the dark, and then, immediately after 30 minutes of 1 sun light exposure under open-circuit. According to Mahesh, et. al.⁴, one of the indications for halide segregation is the appearance of a large shoulder in the region close to the exponential absorption onset of the EQE at $\sim 10^{-2}$. This shoulder represents a redshift in the onset which means that the light is being absorbed by the low gap (iodine) domains. This shifting is enhanced by the exposure of the cell for several minutes to a 1 sun equivalent illumination. However, here no significant shoulder appears after 30 minutes like soaking suggesting that the halide segregation is small in volume despite the dominance of the redshifted emission in PL. We note, that this does not exclude that there is in fact a feature at EQE values of $\leq 10^{-4}$ or at lower energies.



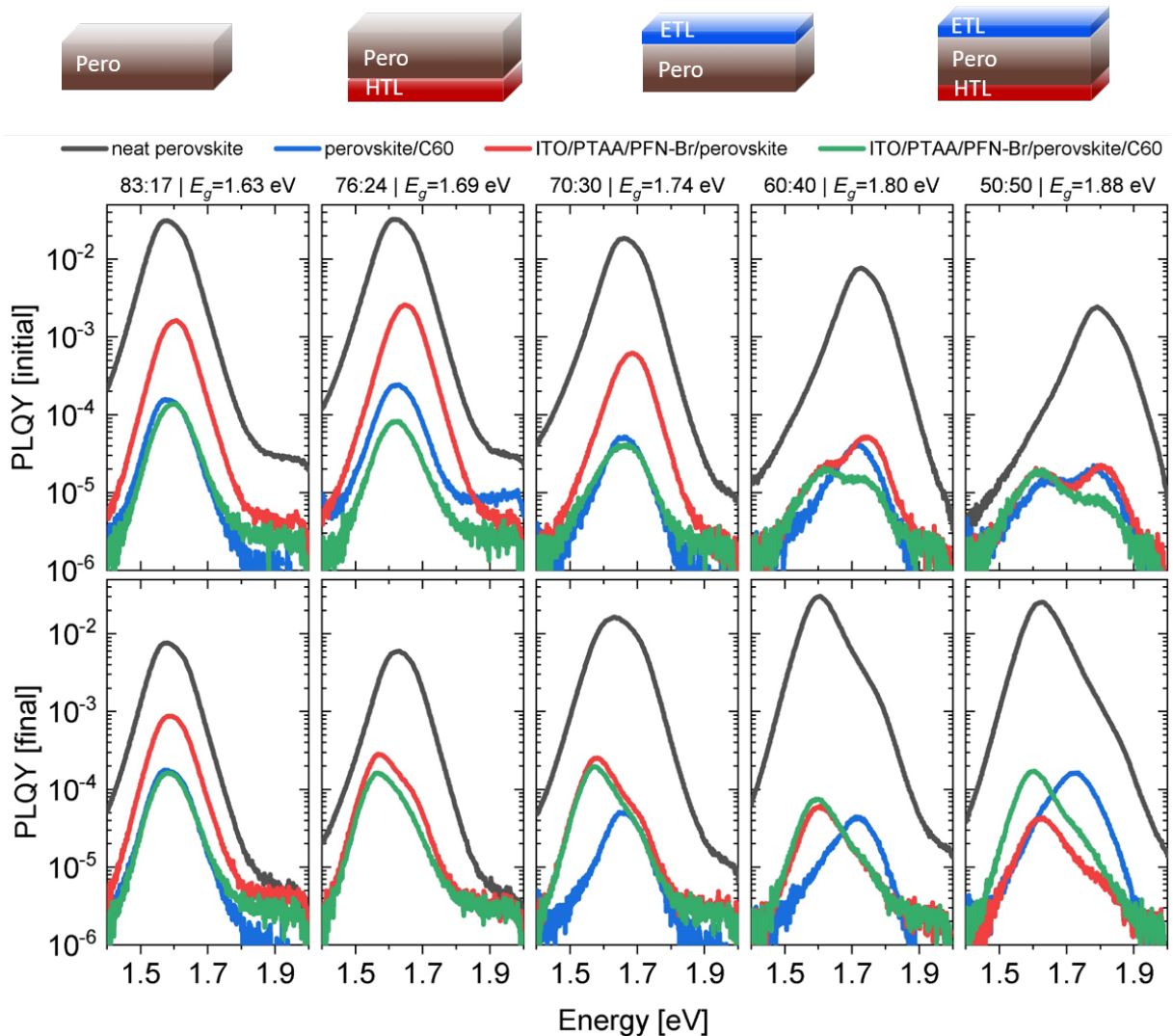
Supplementary Figure S2. Performance of the fabricated devices over time. The first measurement was done on 09 January 2020, when the cells were fresh, and the last one on 07 April 2020. The x-labels indicate the composition of corresponding triple cation $CS_{0.05}(FA_xMA_y)_{0.95}Pb(I_xBr_y)_3$ cells. The figures shows the stability of the cells kept in the dark since their fabrication until now. The trend of every parameter is the same for both the dates. The subtle differences in PCE are mainly due to the fill factor decrease.



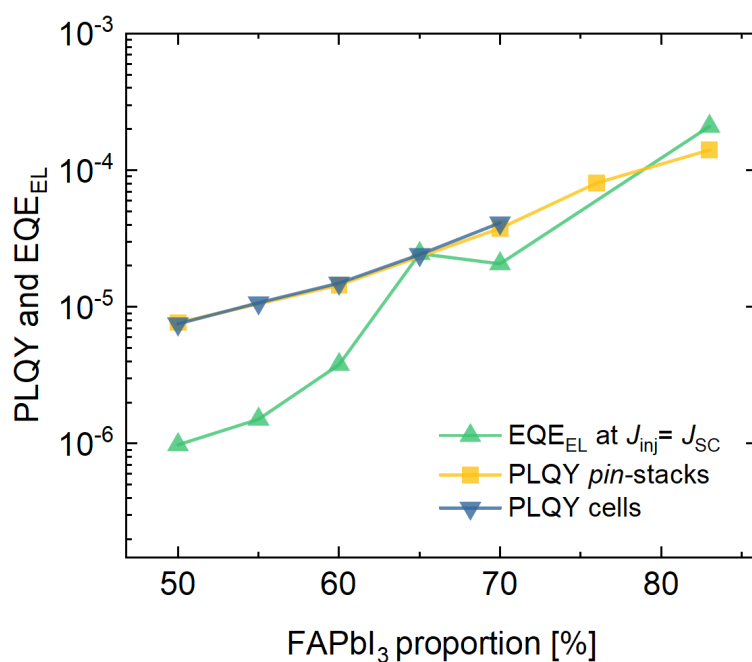
Supplementary Figure S3. Short-time maximum power point (MPP) tracking of 3 selected triple cation $CS_{0.05}(FA_xMA_y)_{0.95}Pb(I_xBr_y)_3$ cells. While the cells with a Br-content of 24% and 40% are stable on these timescales, the 50% Br containing device displays a continuous decrease in PCE due to the severe halide segregation in this sample.



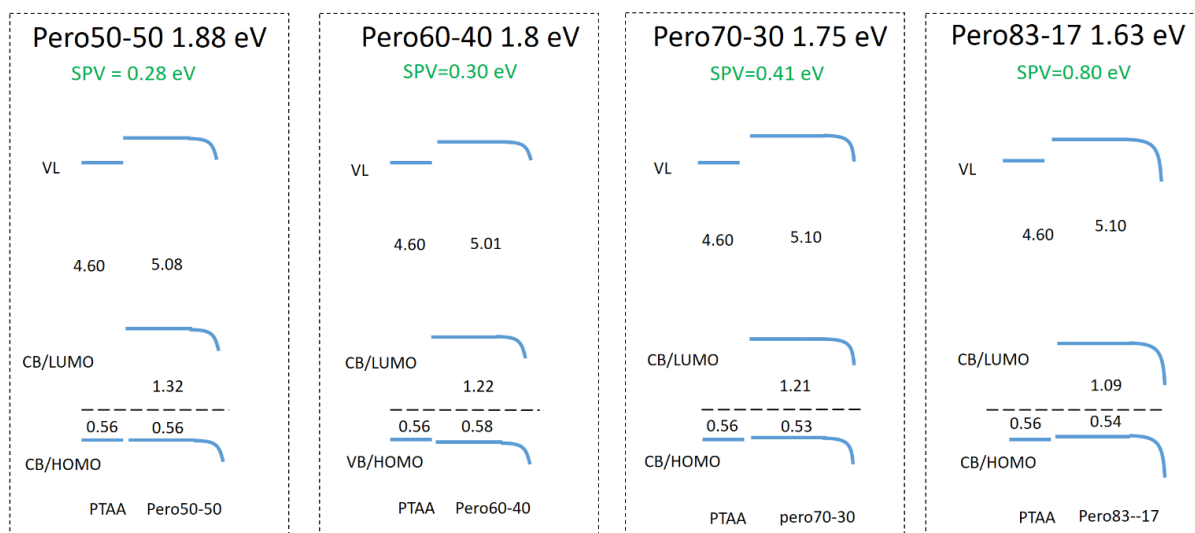
Supplementary Figure S4. **a**, Original electroluminescence spectra of the different $\text{Cs}_{0.05}(\text{FA}_x\text{MA}_{1-x})_{0.95}\text{Pb}(\text{I}_x\text{Br}_{1-x})_3$ wide bandgap perovskites solar cells in a log-linear representation at a voltage of 1.2 V. **b**, Electroluminescence quantum yield (EQE_{EL}) as a function of injected current density for the selected compositions. The highlighted data points represent 1 Sun conditions, i. e. where the injected current equals the short-circuit current.



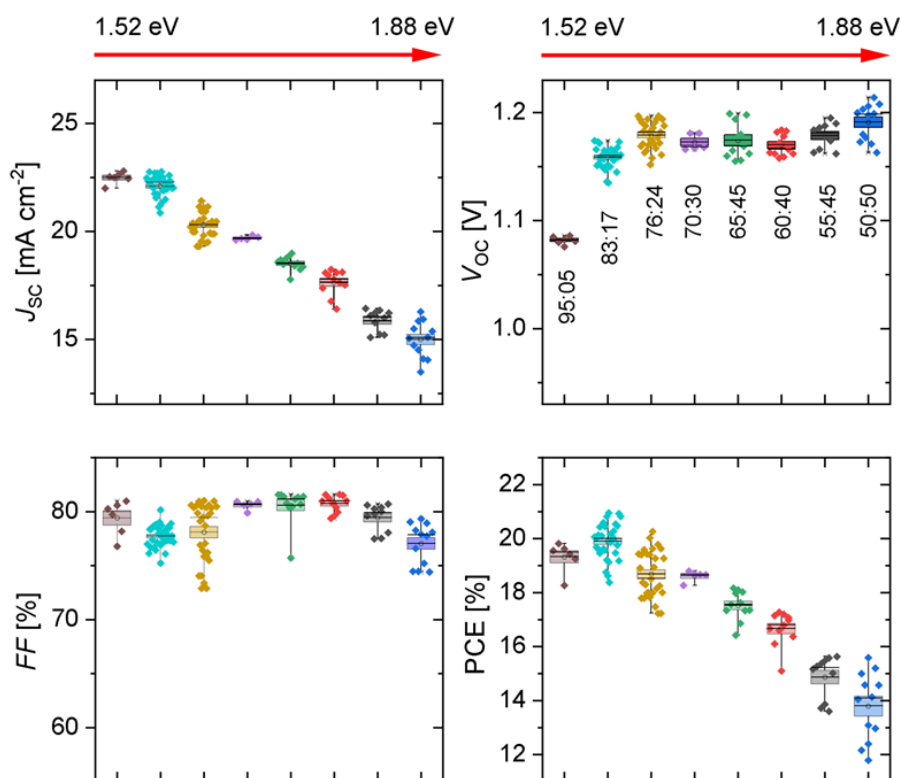
Supplementary Figure S5. PL of different stack layers, after a few seconds (initial) and after a few minutes of illumination which promotes the halide segregation (final). While both interfaces are problematic in Br-rich samples, the results also show that perovskite/ C_{60} films (blue) segregate slower than all other films (i.e. all films with PTAA and the neat perovskite). However, unfortunately, the presence of C_{60} cannot stop the segregation in the complete *pin*-stack (green).



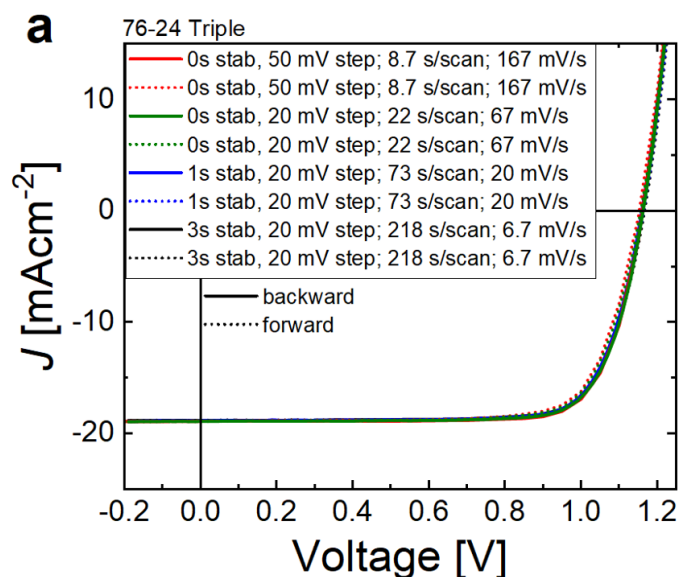
Supplementary Figure S6. The initial PLQY (~after 1 s illumination) of the cells and the *pin*-stacks compared to the device EQE_{EL} considering the emission from the mixed halide phase. At a FAPI to MAPbBr₃ ratio of 50:50, the EQE_{EL} is approximately 1×10^{-6} , while the PLQY of the *pin*-stacks on glass and the complete cell are both around $\sim 7.5 \times 10^{-6}$. This indicates that the internal QFLS is around ~ 53 mV larger than the external V_{OC} in the 50:50 triple cation cell.



Supplementary Figure S7. Possible band diagram of the wide-gap, Br-rich perovskite cells as deduced from ultraviolet photoelectron spectroscopy measurements. The energy levels of the hole transport and perovskite layer were obtained by measuring the top surface of ITO/PTAA:PFN and ITO/PTAA:PFN/perovskite films, respectively. The graph shows the valence band onset with respect to the Fermi level of the ITO substrate, while the optical gap of the perovskites was added to obtain the conduction bands. In order to flatten the internal band bending in the HTL/perovskite films (i.e. the built-in field), the samples were illuminated using a roughly 1-sun equivalent light source that saturates the shift in the valence band spectra with increasing intensity. This allows to assess the energy levels under “flat band” conditions. We attribute the internal band bending in the perovskite to a *n*-type surface due to the presence of donor-type surface states possibly consisting of metallic Pb.^{3,5} However, we also note, that the origin of the photo-voltage remains as a heavily debated topic,⁶ for example, the band bending could also occur at the buried bottom interface.^{7,8} Moreover, the spatial extend of the bending is unknown, which depends on the doping of the perovskite. In any case, the field facilitates photocarrier extraction (holes to the HTL, or electrons to the ETL) and we found that it increases with decreasing Br-content. Importantly, all perovskites exhibit similar values of work function and valence band onset under saturated illumination condition, demonstrating a rather constant ionization energy of the mixed perovskites. Importantly, the valence band onset of the perovskite under illumination matches with the valence band onset of PTAA. Therefore, these measurements suggest that there is no significant energy offset at the *p*-interface, which is consistent with the relatively small mismatch between the PLQY and EQE_{EL} in **Supplementary Figure S6**.

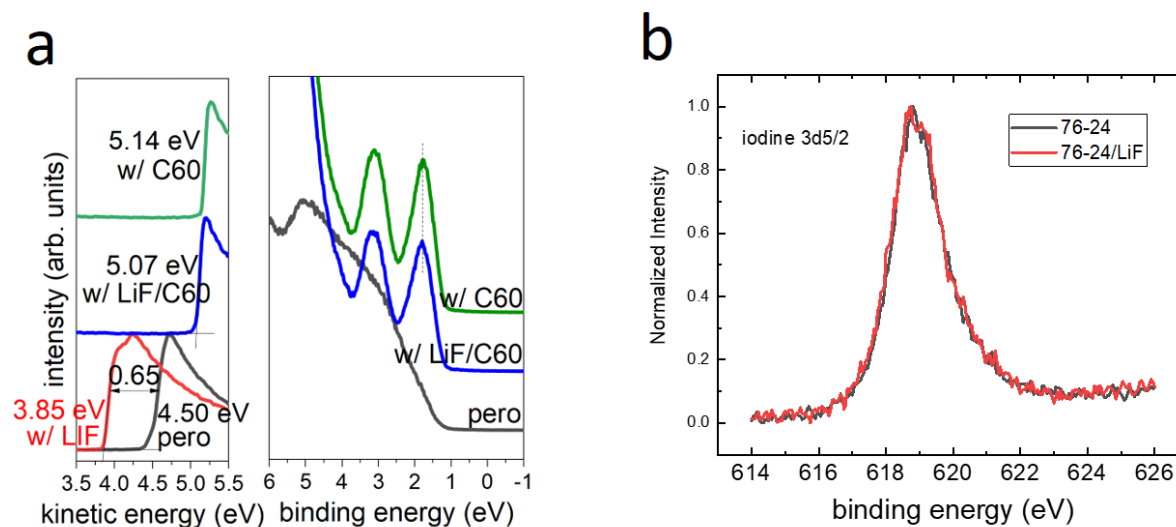


Supplementary Figure S8. Average performance parameters of the $\text{Cs}_{0.05}(\text{FA}_x\text{MA}_y)_{0.95}\text{Pb}(\text{I}_x\text{Br}_y)_3$ triple cation perovskite cells with LiF.



Supplementary Figure S9. Forward and backward JV -scans (hysteresis) at different scan speeds exemplified on a freshly prepared 76-24 triple cation cells. The stabilization (“stab”) time at each voltage, the voltage step size, the duration per scan in one direction and the resulting scan speed are specified in the figure legend. The scan rate is varied from 167 mV/s to 6.7 mV/s which means the scan speed is changed by a factor of 25. Generally, we observe a comparatively small hysteresis in these pin -type devices, which might be however more pronounced at even faster scan speeds. The fastest

scan speed of our solar simulator setup is around ~ 300 mV/s when aiming to keep a sufficient voltage resolution (50 mV).



Supplementary Figure S10. **a**, UPS spectra on different stack layers of $\text{Cs}_{0.05}(\text{FA}_x\text{MA}_y)_{0.95}\text{Pb}(\text{I}_x\text{Br}_y)_3$ with $x=76$, $y=24$ triple cation perovskite with a bandgap of 1.69 eV. The measurements demonstrate the creation of a significant reduction of the perovskite workfunction (Wf) upon application of LiF. **b**, The identical iodine 3d5/2 core levels of the perovskite suggest that the reduction of the workfunction is due to the formation of a surface dipole. Otherwise, if doping were responsible for the Wf shift, the change in the local electrostatic potential would shift the atomic energy levels, the work functions, valence bands and core levels, which is not observed here. Notably, the reduction of the workfunction significantly increases the PL of the neat perovskites, the perovskite/ C_{60} stack and the device V_{OC} as it creates a barrier for minority carriers to reach the C_{60} layer.

Supplementary References

- (1) Endres, J.; Egger, D. A.; Kulbak, M.; Kerner, R. A.; Zhao, L.; Silver, S. H.; Hodes, G.; Rand, B. P.; Cahen, D.; Kronik, L.; Kahn, A. Valence and Conduction Band Densities of States of Metal Halide Perovskites: A Combined Experimental-Theoretical Study. *J. Phys. Chem. Lett.* **2016**, *7*, 2722–2729.
- (2) Zu, F.; Amsalem, P.; Egger, D. A.; Wang, R.; Wolff, C. M.; Fang, H.; Loi, M. A.; Neher, D.; Kronik, L.; Duhm, S.; Koch, N. Constructing the Electronic Structure of $\text{CH}_3\text{NH}_3\text{PbI}_3$ and $\text{CH}_3\text{NH}_3\text{PbBr}_3$ Perovskite Thin Films from Single-Crystal Band Structure Measurements. *J. Phys. Chem. Lett.* **2019**, *10*, 601–609.
- (3) Zu, F.; Wolff, C. M.; Ralaarisoa, M.; Amsalem, P.; Neher, D.; Koch, N. Unraveling the Electronic Properties of Lead Halide Perovskites with Surface Photovoltage in Photoemission Studies. *ACS Appl. Mater. Interfaces* **2019**, *11*, 21578–21583.
- (4) Mahesh, S.; Ball, J. M.; Oliver, R. D. J.; McMeekin, D. P.; Nayak, P. K.; Johnston, M. B.; Snaith, H. J. Revealing the Origin of Voltage Loss in Mixed-Halide Perovskite Solar Cells. *Energy Environ. Sci.* **2020**, *13*, 258–267.
- (5) Zu, F. S.; Amsalem, P.; Salzmann, I.; Wang, R. Bin; Ralaarisoa, M.; Kowarik, S.; Duhm, S.; Koch, N. Impact of White Light Illumination on the Electronic and Chemical Structures of Mixed Halide

and Single Crystal Perovskites. *Adv. Opt. Mater.* **2017**, *5*.

- (6) Luo, D.; Yang, W.; Wang, Z.; Sadhanala, A.; Hu, Q.; Su, R.; Shivanna, R.; Trindade, G. F.; Watts, J. F.; Xu, Z.; Liu, T.; Chen, K.; Ye, F.; Wu, P.; Zhao, L.; Wu, J.; Tu, Y.; Zhang, Y.; Yang, X.; Zhang, W.; Friend, R. H.; Gong, Q.; Snaith, H. J.; Zhu, R. Enhanced Photovoltage for Inverted Planar Heterojunction Perovskite Solar Cells. *Science* **2018**, *360*, 1442–1446.
- (7) Olthof, S.; Meerholz, K. Substrate-Dependent Electronic Structure and Film Formation of MAPbI₃ Perovskites. *Sci. Rep.* **2017**, *7*, 1–10.
- (8) Daboczi, M.; Hamilton, I.; Xu, S.; Luke, J.; Limbu, S.; Lee, J.; McLachlan, M. A.; Lee, K.; Durrant, J. R.; Baikie, I. D.; Kim, J.-S. Origin of Open-Circuit Voltage Losses in Perovskite Solar Cells Investigated by Surface Photovoltage Measurement. *ACS Appl. Mater. Interfaces* **2019**, *11*, 46808–46817.